Optical Materials 109 (2020) 110348

Contents lists available at ScienceDirect

Optical Materials

journal homepage: http://www.elsevier.com/locate/optmat

Short Communication

Role of defects in modulating the near band edge emissions of sub-micron ZnO crystals

Prashant A. Borade [a], Tushar Sant [a], Anisha Gokarna [b], Kapil U. Joshi [c], Rahul P. Panat [d,**], S. M. Jejurikar [a,*]

[a] National Centre for Nanoscience and Nanotechnology, University of Mumbai, Kalina Campus, Santacruz (E), Mumbai, 400098, India
[b] Laboratory Light, nanomaterials and nanotechnologies – L2n, University of Technology of Troyes & CNRS ERL 7004, 12 rue Marie Curie, CS 42060, 10004, Troyes Cedex, France
[c] Anton-Paar India Pvt. Ltd, Thane (W), 400607, India
[d] Department of Mechanical Engineering, Carnegie Mellon University, Pittsburgh, PA, 15213, USA

ARTICLE INFO

Keywords:
ZnO
CBD
Rods
Tubes
Photoluminescence (PL)
Near band-edge emission (NBE)

ABSTRACT

In this communication, we identify the role of defects in modulating the optical properties of ZnO sub-micron rod and tube structures by measuring and comparing their temperature dependent (18 K–260 K) photoluminescence (PL) behavior. From statistical fitting of the near band edge (NBE) emission region of the spectra, it is observed that the acceptor exciton (A, X) emissions decrease with an increase in temperature for ZnO rod structures, whereas comparatively less variation is recorded for ZnO tubular structures. Employing various mathematical analyses, the emission patterns observed for tubular structures are concluded to arise from their lattice dilation and the electron-phonon interactions. For the rod structures, however, it is concluded that the emission spectra are primarily due to the defects (i.e. oxygen and/or Zn vacancies) present at their polar faces. The defects present at the ZnO basal plane affecting (A, X) emissions will influence the use of ZnO in optoelectronic applications.

1. Introduction

The study of growth and characterization of ZnO crystals has gained popularity due to their exclusive properties such as large exciton binding energy (60 meV at room temperature) when compared to GaN (26 meV) and ZnSe (20 meV) [1]. Zinc oxide also has a high degree of transparency (>90%) to visible light, easily achievable n-type conductivity [2], non-toxicity, and bio-compatible behavior [3]. These properties, in addition to the abundance of its constituent elements, have made ZnO a potential candidate for optical and optoelectronic applications such as light emitting diodes, optical emitters, surface coatings, transparent conducting coatings (TCO) and quantum mechanical systems. Various forms of ZnO have been already reported which include bulk crystals, thin films and various 1D-2D nanostructures [4]. Sub-micron ZnO crystals have generated a significant interest due to their advantages over thin films or bulk crystals such as a) high aspect ratio and large surface area to volume ratio that reduces the dislocation densities, b) small footprint and large free surfaces that help relieve the stresses induced by thermal mismatch, and c) quantum confinement which may enhance the radiative recombinations to emit light in the ultraviolet (UV) spectral range. Zinc oxide nanorods exhibit quantum confinement which can significantly enhance the exciton binding energy [5].

It has been demonstrated that the intrinsic defects (vacancies, interstitials and their associates) play an important role in shaping the electronic and optical properties of ZnO [6]. The typical optical emission recorded from ZnO can be categorized as that in the UV (i.e. Near Band Edge or NBE) and in the visible range. Several mechanisms have been proposed to explain the visible emissions observed so far, attributing these emissions to the vacancies, surface defects, and the morphology of the crystal [7–14]. Presences of such defects are observed to produce number of bands within the band gap producing visible luminescence. For example, green emission observed is due to two bands - one due to excess Zn and the other due to the residual impurities [4,8]. Excess oxygen present in ZnO caused by specimens annealed in oxygen or air was observed to result in self-activated orange emissions [15]. For high quality ZnO crystals, the UV emission is observed to be more intense than the visible emission. Though several peaks and shoulders are always observed to be present in the UV region, only a few of them have

* Corresponding author.
** Corresponding author.
E-mail addresses: rpanat@andrew.cmu.edu (R.P. Panat), suhas.j@nano.mu.ac.in (S.M. Jejurikar).

https://doi.org/10.1016/j.optmat.2020.110348
Received 12 June 2020; Received in revised form 10 August 2020; Accepted 17 August 2020
Available online 31 August 2020

been studied so far. The UV-emission (i.e. NBE) is thus believed to be a result of radiative recombination process between the photo-generated electrons from the conduction band and holes generated in the valence band (i.e. free excitons), the bound excitons, longitudinal optical (LO) phonon replicas, and the donor-acceptor-pair (DAP) transitions [16,17]. Emissions observed due to the bound excitons commonly termed as extrinsic transitions, which are because of the discrete electronic states created in the band gap by native defects, complexes, or dopants present in the crystal [18]. Thus in literature, the emission peaks positioned at 3.365 eV and 3.353 eV are ascribed to the excitons bound to neutral donors (D^oX) and acceptors (A^oX), respectively [19,20]. In addition, the peaks positioned at 3.30 eV and 3.228 eV are identified as donor pair acceptor transitions (DAP) and first order DAP-LO [21]. The time resolved NBE PL investigation reported by Reparaz et al. [22] shows that the increase in the life time of the neutral bound exciton (3.365 eV) as a function of diameter of ZnO nanowires was due to their high surface-to-volume-ratio. Further Rauch et al. [23]. have claimed that the free electron to bound hole transitions (e^-, A^oX) are the transitions related with the intersection of basal plane defects present on the material surface. Application wise, however, the presence of defects (i.e. emission centers) is observed to adversely impact the optical performance of ZnO-based optoelectronic and electronic devices [24,25]. In order to improve the performance of these devices, it is essential to gain a fundamental knowledge of the effect of defects on the optical properties of ZnO. Further, knowing the fact that crystal morphology plays an important role in controlling the optical properties of ZnO nano/micro crystals, a very limited information is available to our knowledge that defines the exact role played by these defects present at polar faces on ZnO optical properties.

The purpose of undertaking this work is thus twofold. First, we aimed to characterize two types of ZnO microstructures with different defect morphologies by measuring their temperature dependent photoluminescence properties [26]. The rod and tube shaped ZnO sub-micron structures were fabricated following our previous work, where the difference in their morphology was known to be due to stacking defects, followed by photoluminescence spectroscopy between 18 K and 260 K. The second aim was to quantify the contribution of the defects on optical emission, especially the Near Band Edge (NBE) and the deep level emissions via theoretical modeling of the experimental observations. The focus was on using Manoogian- Leclerc and Bose-Einstein models applied to the experimental observations to quantify the exact defect mechanism for observed luminescence from these structures.

2. Experimental

The process of ZnO rods and tubes is described in our earlier work [26] but included here for completeness. Hexagonal ZnO rods were grown on SiO_2/Si substrate by chemical bath deposition (CBD) route using molar concentration of zinc acetate dihydrate and sodium hydroxide (S. D. Fine Chemicals, India, 99% purity) prepared in DI water. Under steady stirring, NaOH (2 M) solution was added drop-by-drop into a 200 ml solution of zinc acetate (0.1 M) until the pH of the solution reached 7. Before the deposition, substrates were cleaned ultrasonically using trichloroethylene, acetone, isopropyl alcohol, and DI water. The growth of ZnO rods was achieved by dipping substrates into the above solution for 80 min at 80 °C. Tube structures were synthesized by exposing some of the rod samples (i.e. hexagonal rods) to the evaporate emerging from the same solution by placing them 3 mm above the solution meniscus for 40 min. The specimens thus produced were washed with ethanol and DI water several times and finally dried at 100 °C for 2 h in air. Morphological and structural investigation of the synthesized specimens were performed using X-ray diffraction (XRD) (Model Ultima IV, Rigaku Corporation, Japan), Scanning Electron Microscope (SEM) (FEI-Inspect F50, FEI Corporation, USA), and Transmission Electron Microscope (TEM) (FEI-Tecnai G2 F30 ST, FEI Corporation, USA) to validate the synthesis. Temperature dependent optical investigations were performed using photoluminescence (PL) technique using an Acton Spectra-pro 2750 ultraviolet–visible spectrophotometer (Princeton Measurements, USA) and a He–Cd laser as an excitation source along with a 350 nm filter.

3. Results and discussion

Fig. 1a shows the XRD of the ZnO rod structures which confirms the formation of single-phase Wurtzite ZnO [27]. Typically, in Wurtzite ZnO, each anion is surrounded by four cations at the corners of a tetrahedron and vice versa via sp^3 covalent bonding. Fig. 1b shows the stick and ball stacking model (top view) for Wurtzite ZnO.

The crystal is considered to form of number of alternating planes composed of four-fold coordinated cations and anions stacked alternatively along c-axis (Fig. 1b) [28,29]. The typical arrangement of anions and cations thus leads to form characteristic planes (i.e. polar and non-polar planes) of the crystal as shown in Fig. 1c. The polar plane (i.e. (0001)) of the crystal is positively charged if it starts with the Zn termination, whereas if it starts with the O termination (i.e. $(000\bar{1})$), it is negatively charged. Alongside of these two primary planes there are multiple secondary non-polar of ZnO Wurtzite crystals shown as Fig. 1c [30].

Fig. 1d,e shows SEM and TEM images of ZnO rod structures that have shapes of truncated hexagonal pyramids and dumbbells. Fig. 1f,g shows SEM images of tube structures with the tube wall thickness of about 25 nm. According to the growth model proposed by researchers [31], the basal plane is observed to be the most favorable surface in order to grow and etch the crystal, generate defect, to define the piezoelectricity etc. Thus, Fig. 1h shows the TEM image recorded on the tube structure confirming the selective etching of as-grown rods. The crystal lattice fringes present in HRTEM image (Fig. 1i) are observed to have fringe spacing value equal to the 'd' spacing values of (101) crystallographic planes of ZnO [24]. Thickness of the side walls (i.e. non-polar faces) of these structures are observed to depend on the size of the pristine rods. Higher concentration of molecular and structural defects (such as excess Zn^{2+}, steps, etc.) present at the polar surface make the surface highly reactive. Dissociation of water molecule at these surfaces produces OH^- and H^+ ions essential for decomposing rods at their polar surfaces. The mechanism related to the transformation of ZnO rods into its tubular structures, which includes selective removal of the stacking defects (e.g. steps, vacancies, Zn terminated surfaces) present at the polar surface has been reported in our earlier work [26].

The temperature dependent PL spectra recorded at 18 K, 25 K, 50 K, 75 K, 100 K, 120 K, 140 K, 160 K, 180 K, 200 K, 220 K and 260 K for the ZnO rod and tube structures specially focusing in the UV region are shown as Figs. 2 and 3, respectively. We deconvolute the PL spectra at 300 K and 18 K due to the broad and asymmetric nature of the graphs as shown in Figs. S1a and S1b, respectively, provided as supporting information. From the spectra recorded for both the structures at 300 K (Fig. S1a), it is observed that the intensity of NBE emission is greater than the intensity of the visible emission. The intensity ratio (i.e. $I_{visible}/I_{NBE}$) calculated for rod and tube structures is observed to be 0.49 and 0.37, respectively. This indicates [32,33] that the presence of any other impurities due to the adopted synthesis process are not significantly influencing the ZnO defect density associated with our structures. However, the possible presence of Na in ZnO at low concentrations ($x \leq 0.2$) acts as a shallow acceptor by occupying position at the substitutional sites [34–36], whereas its presence in excess amount ($x \geq 0.2$) is observed to increase density of oxygen vacancies [37]. Thus, the presence Na in ZnO primarily affects the emissions in the visible region (blue and green region) via radiative recombination processes [33]. However, the exact role of impurities such as Na in ZnO still remains unclear and will be goal of a future investigation.

As expected, the UV peak recorded herewith is observed to broaden and shift towards higher wavelength with an increase in temperature.

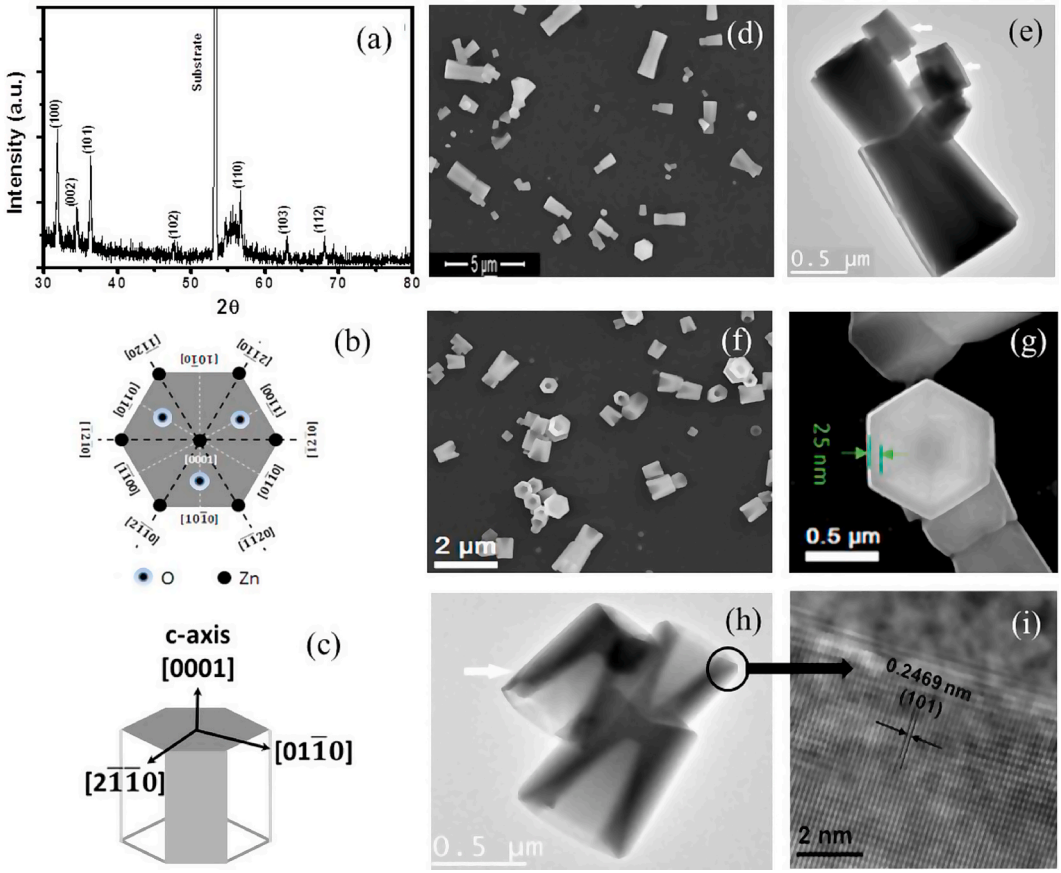

Fig. 1. ZnO sub-micron crystals. (a) XRD pattern, (b) stick and ball model (top view) for Wurtzite crystal structures of ZnO, (c) polar and nonpolar surfaces of ZnO Wurtzite crystal (d,e) SEM and TEM images of ZnO (hexagonal) rods, respectively. (f,g) SEM at different magnifications and (h, i) TEM and HRTEM images of ZnO tubes.

Similar to the previous exercise due to the asymmetric nature of the peak, the spectra are deconvoluted into multiple peaks. Depending on the peak position observed, they are assigned to (FX_A), (D, X), (A, X) and/or "Y" band emissions or excitons bound to Na in ZnO [6,29,38,39], respectively (Section S1 of supporting information).

Comparing Figs. 2 and 3, it is clear that the FX_A peak (i.e. free excitonic transition) is present only in the case of rod structures and is observed to maintain the same peak position throughout the temperature range. For both these structures, the (D, X) and (D, X)-LO emissions are observed to shift towards the higher wavelength with the rise in temperature as already reported by others. Similar trend is recorded for the (A, X) emission in the case of rod structures, whereas less variation observed with (A, X) peak position for tube structure make the finding fascinating.

To confirm the observed emission behavior from both the structures, we tried to fit the red shifts particularly for (D, X) and (A, X) emissions as a function of temperature using Varshni's equation, which is expressed as [38,41],

$$E_x(T) = E_x(0) - \frac{\alpha T^2}{(T+\beta)}, \tag{1}$$

where $E_x(0)$ is band energy at absolute zero, T is the temperature, and α and β are model parameters. The Varshni's model shows a decrease in the (D, X) and (A, X) peak energy with a rise in temperature (Fig. 4).

It is important to note that the energy variation of (A, X) peak especially for the tube structure (Fig. 4b), indicates some abnormality with the particular emission. The peak position is observed to remain almost constant up to a temperature of 120 K, and then suddenly decreases with a rise in temperature. It has been already proposed that the red shifts associated with these emissions are primarily due to lattice dilation and the electron phonon interactions [42]. A suitable model which accounts the lattice distortive (dilation and/or shear) effect along with the electron phonon interaction has been proposed by Manoogian et al. [43], which is expressed as below,

$$E_x(T) = E_x(0) - UT - \frac{\alpha\Theta}{\exp(\Theta/T) - 1} \tag{2}$$

where $E_x(0)$ is the band energy at absolute zero, U is the coefficient of lattice expansion, Θ is the averaged phonon energy, α is a coupling constant (associated with the strength of electron-phonon interactions) and T is the absolute temperature.

Fig. 5a and b shows the theoretical fits executed using the Manoogain-Leclerc model (Eq. (2)) for the (D, X) and (A, X) peak energy with respect to increase in temperature for the ZnO rod and tube structures. Excellent theoretical fit with the experimental data for both the peak energies in both the structures is observed. The fitting parameters extracted from the exercise are listed in Table 1 below, which are observed to be comparable with the parameters reported by others [44].

From the values of fitting parameters, obtained using the model which especially considers the lattice dilation (i.e. "U"), the values reported here are comparable with other reports [45,46] and it can be claimed that the emissions are governed by the lattice dilation as well as the phonon interactions for both these structures. However, to confirm the exact role of lattice dilation, we use Bose-Einstein model with the experimental data, noting that this model takes into account only the electron-phonon interactions [47]. The model is expressed as,

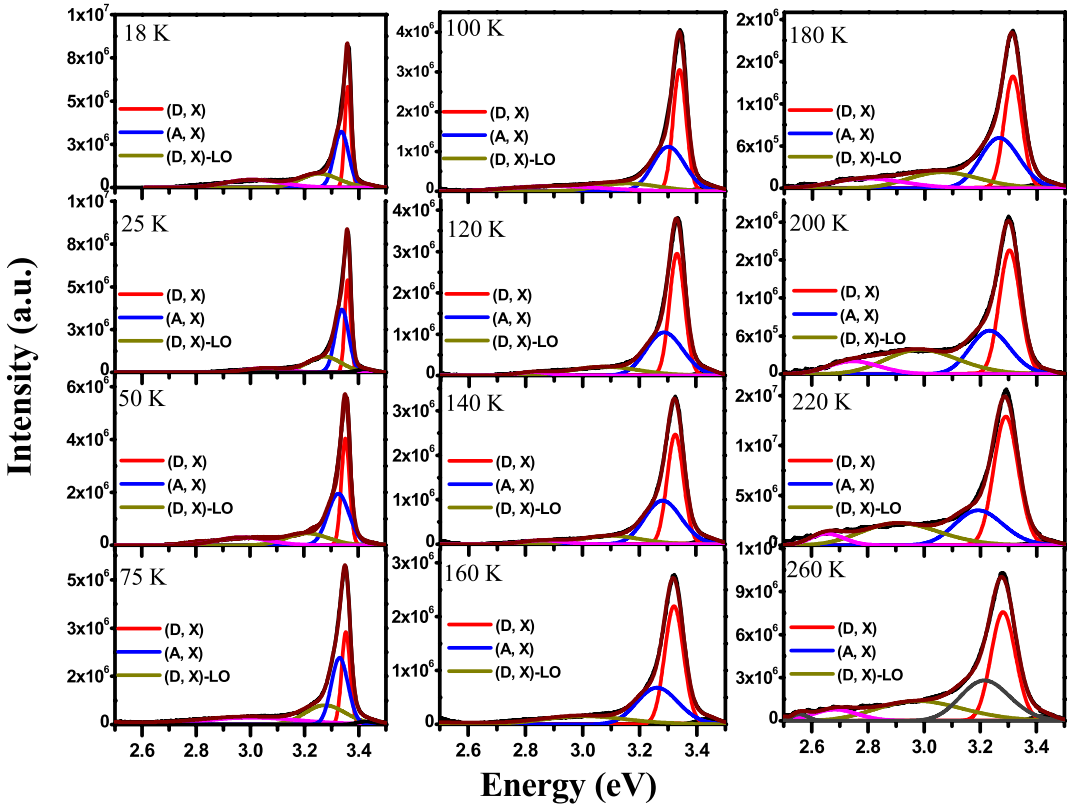

Fig. 2. Temperature dependent PL spectra (Jacobian-corrected intensity [40]) deconvoluted with (FX_A), (D, X), (A, X) and/or "Y" band peak positions for ZnO rod structures.

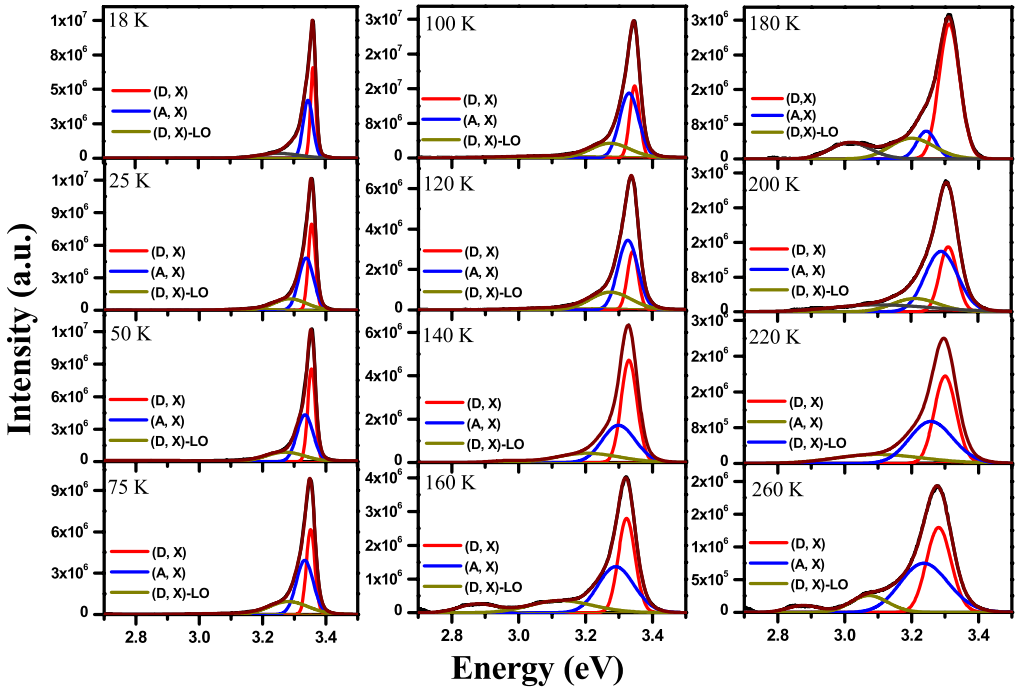

Fig. 3. Temperature dependent PL spectra (Jacobian-corrected intensity [40]) deconvoluted with (FX_A), (D, X), (A, X) and/or "Y" band peak positions for ZnO tube structures.

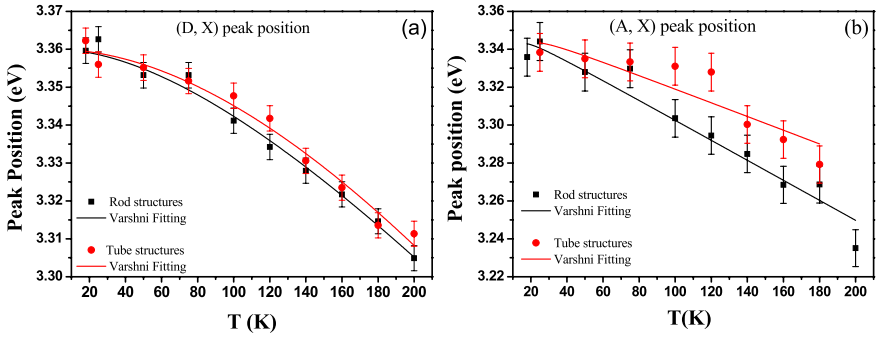

Fig. 4. Varshni's Model fitting for (a) (D, X) peak position variation and (b) (A, X) peak position variation with respect to temperature for ZnO rod and tube structures.

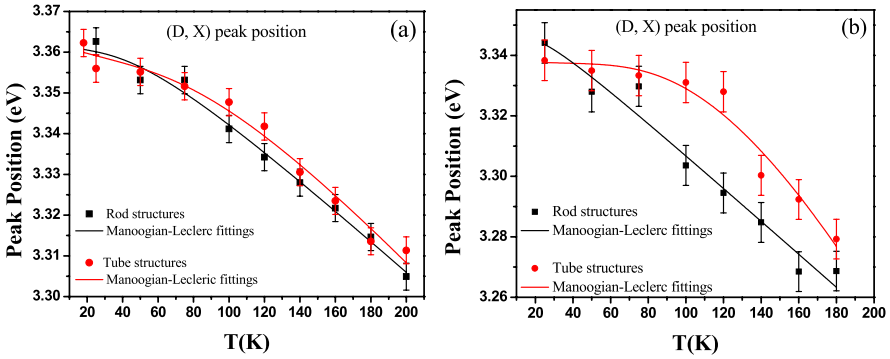

Fig. 5. Manoogian-Leclerc Fitting for (a) (D, X) peak position variation and (b) (A, X) peak position variation with respect to temperature for rod and tube structures.

Table 1
Fitting parameters extracted for NBE emissions observed for rod and tube structures using Manoogian-Leclerc (Eq. (2)) and Bose-Einstein model (Eq. (3)).

Model used	Parameters	NBE Emission investigated			
		Rod structures		Tube structures	
		(D, X)	(A, X)	(D, X)	(A, X)
Manoogian- Leclerc Model	$E_g(0)$**eV**	3.367 ± 0.005	3.350 ± 0.012	3.361 ± 0.003	3.336 ± 0.011
	U	2.32×10^{-4}	3.45×10^{-4}	0.99×10^{-4}	0.52×10^{-4}
		$(\pm 3.4 \times 10^{-5})$	$(\pm 6.9 \times 10^{-5})$	$(\pm 2.1 \times 10^{-5})$	$(\pm 3.4 \times 10^{-5})$
	α (eV/K)	2.05×10^{-4}	2.59×10^{-4}	4.01×10^{-4}	1.43×10^{-3}
		$(\pm 7.9 \times 10^{-5})$	$(\pm 1.5 \times 10^{-5})$	$(\pm 6.2 \times 10^{-5})$	$(\pm 2.3 \times 10^{-5})$
	$\boldsymbol{\theta}$ **(*k*)**	335 ± 20	198 ± 32	312 ± 12	473 ± 14
	χ_R^2	1.06×10^{-6}	7.23×10^{-6}	1.50×10^{-6}	5.40×10^{-6}
Bose-Einstein Mode	$E_g(0)$**eV**	3.362 ± 0.004	3.342 ± 0.021	3.359 ± 0.015	3.342 ± 0.005
	α (eV/K)	3.79×10^{-4}	5.92×10^{-4}	4.38×10^{-4}	12.02×10^{-4}
		$(\pm 2.6 \times 10^{-5})$	$(\pm 1.1 \times 10^{-5})$	$(\pm 5.5 \times 10^{-5)}$	$(\pm 4.8 \times 10^{-5})$
	$\boldsymbol{\theta}$ **(*k*)**	111 ± 20	110 ± 47	204 ± 35	379 ± 95
	χ_R^2	1.05×10^{-6}	1.16×10^{-6}	4.98×10^{-6}	5.38×10^{-6}

$$E_x(T) = E_x(0) - \frac{\alpha\Theta}{\exp(\Theta/T) - 1}, \tag{3}$$

where $E_x(0)$ is band energy at absolute zero, Θ an averaged phonon energy, α a coupling constant (associated with the strength of electron-phonon interactions) and T is the absolute temperature. Figure S3 (supporting information) presents the theoretical fits to the experimental data recorded for emissions observed with these structures using Bose-Einstein equation. Various parameters extracted by the exercise are also listed in Table 1. An excellent theoretical fit is observed for the (D, X) peak energy variation for both the structures. Having obtained more or less the same value of chi^2 (*i.e.* χ_R^2) by applying Bose-Einstein as the Manoogian-Leclerc models, it is clear that the effect of lattice dilation in (D, X) emission can be neglected. *We thus conclude that for both the ZnO submicron structures, i.e., rods and tubes, the (D, X) emissions are governed purely by electron-phonon interactions.* However, the higher value of χ_R^2 observed for (A, X) peak energy variation in experiments when compared to the Manoogian-Leclerc model (Table 1) confirms that these particular emissions are governed by lattice dilation in addition to the electron-phonon interactions. Thus, the Manoogian-Leclerc model

pinpoints the exact parameter which determines the physical behavior and is the suitable model to describe the optical measurements reported for ZnO tubes. The value of 'U' listed in Table 1, especially for (A, X) emissions, show significant differences depending on the morphologies investigated in this work. Higher value of lattice dilation coefficient is observed for rod structures than that for tube structures. Thus, based on these values we believe that the (A, X) emissions in case of tube structure are governed primarily by lattice dilation as well as electron-phonon interactions. However, from previous experimental investigations it has been confirmed that for a typical ZnO particle, 70–80% of the total surface is due to the presence of non-polar facets [48,49]. From the cleavage energy investigations estimated for polar and non-polar facets of ZnO, it has been confirmed that the non-polar facets of the crystal exhibit the lowest possible energy values [50,51]. Fundamentally, the polar surfaces/facets (i.e. the (0001) and $(000\bar{1})$) are unstable and to stabilize them, surface rearrangement of charges between the O and Zn termination surfaces takes place [31,52]. In order to accommodate charge transfer, these surfaces exhibit faceting or massive reconstruction via randomly distributed vacancies, impurity atoms, and/or the presence of charged adsorbets in the surface layer [53,54]. The scanning tunneling imaging performed on the polar (mainly Zn terminated) surfaces indicate presence of small islands and number of pits present on the surfaces [55], whereas Parker et al. [56] reported presence of large terraces with no defects (island and/or pit) present in the STM images recorded on the nonpolar $(10\bar{1}0)$ facets. Further analysis of islands and pit size distribution suggested a decrease of surface Zn concentration affecting the charge transfer to stabilize the surface [55]. Hence, we believe that along with the lattice dilation and electron-phonon interactions, the (A, X) emissions in the case of rod structures are governed by concentration of Zn or O present (30-20% of the total surface contain polar facets) in the basal plane of the crystal.

In order to confirm that the defects indeed contributed to the temperature quenching behavior particularly for (A, X) emission, we decided to study the (A, X) peak intensity variation as a function of temperature. Fig. 6 (b) present the Arrhenius plot extracted from the graph of PL intensity as a function of temperature (Figs. 2 and 3). Under steady state excitation, the spectral intensity (I) for the bound emissions can be expressed as,

$$I = \frac{I_0}{1 + Ae^{-E_a/k_B T}} \tag{4}$$

where E_a is the activation energy, A is fitting parameters and k_B is the Boltzmann constant [51].

Using Eq. (4), the activation energies are extracted from the Arrhenius plots for the ZnO structures. The values of thermal activation energy extracted from Fig. 6 and using Eq. (4) are ~25 and 52 ± 5 meV for the rod and tube structures, respectively. The high activation energy observed for (A, X) emissions in the case of tube structures thus confirms that the emissions are either from the electron-acceptor transition and/or due to intrinsic point defects and the extended structural defects. The claim can be supported by the time decay measurements reported by Camarda et al. [8] for ZnO nanoparticles, where authors determine that the exciton emissions (which are observed to be strongly dependent upon the temperature as well as on ZnO structural parameters) are primarily determined by non-radiative recombination due to high defect density related to the crystal [29,57]. The low thermal activation energy observed in the case of rod structures can be associated with "Y" band i. e. the emissions due to radiative recombination of exciton bound extended structural defects present at the polar face of the rods.

4. Conclusions

Temperature dependent photoluminescence (PL) spectroscopy technique was used to study the effect of the morphology dependency on the optical properties of ZnO crystals. For this purpose, ZnO rods (synthesized using chemical bath route) and ZnO tubes (formed using dissolution process) were studied. Presence of free excitonic peak at the higher energies along with the band edge emissions observed in PL spectra for rod structures at room temperature makes the measurements different from that recorded for tubular structures. Presence of these emissions clearly indicates existence of free as well as bound carrier recombination processes present in the rod structures even at room temperature. Disparity observed in visible region of the PL spectra recorded at room temperature from both the specimens can be attributed to the morphology associated with these structures. In order to understand various recombination processes especially related with the near band-edge emission (NBE), temperature dependent PL investigations were conducted on both of these specimens. From the statistical fitting of NBE spectra, it is observed that free excitonic transition present only in the case of rod structures is maintaining the same peak position with rise in the measurement temperature. For both the specimens (D, X) and (D, X)-LO emissions are observed to get shifted towards higher wavelength side with increase in the temperature. However, the acceptor exciton (A, X) emission peak position is observed to decrease with the increase in measurement temperature for rod structures. Comparatively, less variation is recorded for the same in the case of tubular structures. Employing various mathematical models, the behavior of (A, X) emission observed in tubular structures has been attributed to the lattice dilation and electron phonon interactions, whereas for rod structures it has been attributed to the defects present at the polar faces of the structure. Thus, the experimental evidences reported herewith can help researchers identify the defect-related intrinsic optical behavior as well as to offer new mechanism responsible for the ZnO luminescence properties.

Author contribution

Prashant Borade: Methodology, data acquisition.
Tushar Sant: Software, data curation and investigation.

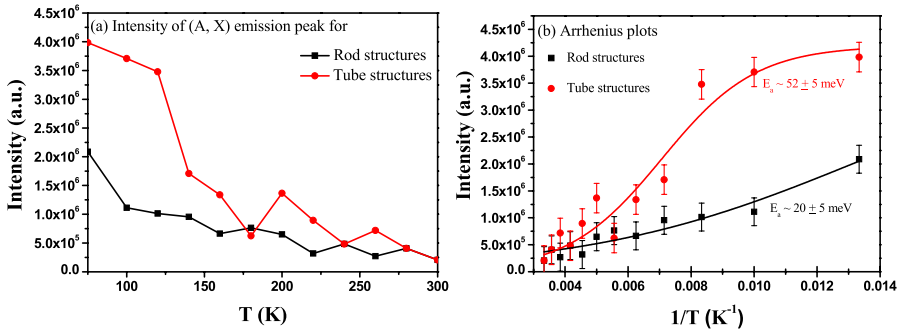

Fig. 6. (a) The temperature dependence of the (Jacobian-corrected [40]) intensity of (A, X) emission peak and (b) Arrhenius plot extracted from Fig. 6 (a) for rod structures and tube structures.

Anisha Gokarna: Investigation and writing original draft.

Kapil Joshi: Data acquisition.

Rahul Panat: Conceptualization, supervision, Writing, Reviewing and Editing.

Suhas Jejurikar: Conceptualization, Supervision and visualization, writing original draft.

Declaration of competing interest

The authors declare that they have no known competing financial interests or personal relationships that could have appeared to influence the work reported in this paper.

Appendix A. Supplementary data

Supplementary data to this article can be found online at https://doi.org/10.1016/j.optmat.2020.110348.

References

[1] D. Thomas, The exciton spectrum of zinc oxide, J. Phys. Chem. Solid. 15 (1–2) (1960) 86–96.
[2] W. Tang, D. Cameron, Aluminum-doped zinc oxide transparent conductors deposited by the sol-gel process, Thin Solid Films 238 (1) (1994) 83–87.
[3] A. Sirelkhatim, et al., Review on zinc oxide nanoparticles: antibacterial activity and toxicity mechanism, Nano-Micro Lett. 7 (3) (2015) 219–242.
[4] Ü. Özgür, et al., A comprehensive review of ZnO materials and devices, J. Appl. Phys. 98 (4) (2005) 11.
[5] Y. Gu, et al., Quantum confinement in ZnO nanorods, Appl. Phys. Lett. 85 (17) (2004) 3833–3835.
[6] A. Uklein, et al., Nonlinear optical response of bulk ZnO crystals with different content of intrinsic defects, Opt. Mater. 84 (2018) 738–747.
[7] H.-L. Guo, et al., Oxygen deficient ZnO 1− x nanosheets with high visible light photocatalytic activity, Nanoscale 7 (16) (2015) 7216–7223.
[8] P. Camarda, et al., Luminescence mechanisms of defective ZnO nanoparticles, Phys. Chem. Chem. Phys. 18 (24) (2016) 16237–16244.
[9] R. Gurwitz, R. Cohen, I. Shalish, Interaction of light with the ZnO surface: photon induced oxygen “breathing,” oxygen vacancies, persistent photoconductivity, and persistent photovoltage, J. Appl. Phys. 115 (3) (2014), 033701.
[10] T.M. Børseth, et al., Identification of oxygen and zinc vacancy optical signals in ZnO, Appl. Phys. Lett. 89 (26) (2006) 262112.
[11] K. Tam, et al., Defects in ZnO nanorods prepared by a hydrothermal method, J. Phys. Chem. B 110 (42) (2006) 20865–20871.
[12] B. Lin, Z. Fu, Y. Jia, Green luminescent center in undoped zinc oxide films deposited on silicon substrates, Appl. Phys. Lett. 79 (7) (2001) 943–945.
[13] Z. Wang, et al., Green luminescence originates from surface defects in ZnO nanoparticles, Phys. E Low-dimens. Syst. Nanostruct. 35 (1) (2006) 199–202.
[14] J. Lv, C. Li, Evidences of VO, VZn, and Oi defects as the green luminescence origins in ZnO, Appl. Phys. Lett. 103 (23) (2013) 232114.
[15] H.S. Kang, et al., Investigation on the variation of green, yellow, and orange emission properties of ZnO thin film, Superlattice. Microst. 39 (1–4) (2006) 193–201.
[16] M.D. McCluskey, S. Jokela, Defects in zno, J. Appl. Phys. 106 (7) (2009) 10.
[17] B. Meyer, et al., Bound exciton and donor–acceptor pair recombinations in ZnO, Phys. Status Solidi 241 (2) (2004) 231–260.
[18] H. Morkoç, Ü. Özgür, Zinc Oxide: Fundamentals, Materials and Device Technology, John Wiley & Sons, 2008.
[19] D. Reynolds, C. Litton, T. Collins, Zeeman effects in the edge emission and absorption of ZnO, Phys. Rev. 140 (5A) (1965) A1726.
[20] A. Teke, et al., Excitonic fine structure and recombination dynamics in single-crystalline ZnO, Phys. Rev. B 70 (19) (2004) 195207.
[21] A. Galdámez-Martinez, et al., Photoluminescence of ZnO nanowires: a review, Nanomaterials 10 (5) (2020) 857.
[22] J.S. Reparaz, et al., Size-dependent recombination dynamics in ZnO nanowires, Appl. Phys. Lett. 96 (5) (2010), 053105.
[23] C. Rauch, et al., Lithium related deep and shallow acceptors in Li-doped ZnO nanocrystals, J. Appl. Phys. 107 (2) (2010), 024311.
[24] L. Brillson, et al., Dominant effect of near-interface native point defects on ZnO Schottky barriers, Appl. Phys. Lett. 90 (10) (2007) 102116.
[25] D.C. Reynolds, D.C. Look, B. Jogai, Optically pumped ultraviolet lasing from ZnO, Solid State Commun. 99 (12) (1996) 873–875.
[26] P. Borade, et al., The transformation of ZnO submicron dumbbells into perfect hexagonal tubular structures using CBD: a post treatment route, Nanotechnology 27 (2) (2015), 025602.
[27] JCPDS Card No. 04-0831. http://www.crystallography.net/cod/index.php.
[28] Ü. Özgür, V. Avrutin, H. Morkoç, Zinc oxide materials and devices grown by molecular beam epitaxy, in: Molecular Beam Epitaxy, Elsevier, 2018, pp. 343–375.
[29] Z. Li, et al., Lateral growth and optical properties of ZnO microcrystal on sapphire substrate, Opt. Mater. 34 (11) (2012) 1908–1912.
[30] M. Skompska, K. Zarębska, Electrodeposition of ZnO nanorod arrays on transparent conducting substrates–a review, Electrochim. Acta 127 (2014) 467–488.
[31] Z. Shujun, et al., Studies on the growth and defects of GdCa4O (BO3) 3 crystals, J. Cryst. Growth 203 (1–2) (1999) 168–172.
[32] C.-L. Hsu, et al., UV-illumination and Au-nanoparticles enhanced gas sensing of p-type Na-doped ZnO nanowires operating at room temperature, Sensor. Actuator. B Chem. 274 (2018) 565–574.
[33] Y.-w. Li, et al., Electrical and optical properties of Na+-doped ZnO thin films prepared by sol-gel method, in: Sixth International Conference on Thin Film Physics and Applications, International Society for Optics and Photonics, 2008.
[34] C. Park, S. Zhang, S.-H. Wei, Origin of p-type doping difficulty in ZnO: the impurity perspective, Phys. Rev. B 66 (7) (2002), 073202.
[35] R. Viswanatha, et al., Synthesis and characterization of Mn-doped ZnO nanocrystals, J. Phys. Chem. B 108 (20) (2004) 6303–6310.
[36] U. Deekshitha, et al., Effect of Na doping on photoluminescence and laser stimulated nonlinear optical features of ZnO nanostructures, Mater. Sci. Semicond. Process. 101 (2019) 139–148.
[37] J.-J. Lai, et al., Effects of Na content on the luminescence behavior, conduction type, and crystal structure of Na-doped ZnO films, J. Appl. Phys. 110 (1) (2011), 013704.
[38] J. Lv, et al., Temperature-dependent shifts of near band-edge emission and their second-order diffraction for ZnO nanorods, Opt. Mater. 34 (11) (2012) 1917–1920.
[39] E. Tomzig, R. Helbig, Band-edge emission in ZnO, J. Lumin. 14 (3) (1976) 403–415.
[40] J. Mooney, P. Kambhampati, Get the Basics Right: Jacobian Conversion of Wavelength and Energy Scales for Quantitative Analysis of Emission Spectra, ACS Publications, 2013.
[41] Y.P. Varshni, Temperature dependence of the energy gap in semiconductors, Physica 34 (1) (1967) 149–154.
[42] R.J. Mendelsberg, et al., Photoluminescence and the exciton-phonon coupling in hydrothermally grown ZnO, Phys. Rev. B 83 (20) (2011) 205202.
[43] A. Manoogian, A. Leclerc, Determination of the dilation and vibrational contributions to the energy band gaps in germanium and silicon, Phys. Status Solidi 92 (1) (1979) K23–K27.
[44] C.S. Granerød, et al., The temperature-dependency of the optical band gap of ZnO measured by electron energy-loss spectroscopy in a scanning transmission electron microscope, J. Appl. Phys. 123 (14) (2018) 145111.
[45] A. Singh, et al., Suppression of near band edge emission in specially engineered ZnO twin nanorods, Phys. Chem. Chem. Phys. 19 (21) (2017) 14012–14019.
[46] D. Hamby, et al., Temperature dependent exciton photoluminescence of bulk ZnO, J. Appl. Phys. 93 (6) (2003) 3214–3217.
[47] R. Pässler, Semi-empirical descriptions of temperature dependences of band gaps in semiconductors, Phys. Status Solidi 236 (3) (2003) 710–728.
[48] X.-L. Yin, et al., Adsorption of atomic hydrogen on ZnO (101 [combining macron] 0): STM study, Phys. Chem. Chem. Phys. 8 (13) (2006) 1477–1481.
[49] F. Haque, et al., ZnO powders as multi-facet single crystals, Phys. Chem. Chem. Phys. 19 (16) (2017) 10622–10628.
[50] F. Viñes, et al., Hydroxyl identification on ZnO by infrared spectroscopies: theory and experiments, J. Phys. Chem. C 118 (3) (2014) 1492–1505.
[51] A.E. Morales, U. Pal, M.H. Zaldivar, Incorporation of Sb in ZnO nanostructures through hydrothermal process, J. Nanosci. Nanotechnol. 8 (12) (2008) 6551–6557.
[52] A. Wander, et al., Stability of polar oxide surfaces, Phys. Rev. Lett. 86 (17) (2001) 3811.
[53] B. Meyer, D. Marx, Density-functional study of the structure and stability of ZnO surfaces, Phys. Rev. B 67 (3) (2003), 035403.
[54] C. Noguera, Polar oxide surfaces, J. Phys. Condens. Matter 12 (31) (2000) R367.
[55] O. Dulub, U. Diebold, G. Kresse, Novel stabilization mechanism on polar surfaces: ZnO (0001)-Zn, Phys. Rev. Lett. 90 (1) (2003), 016102.
[56] T. Parker, et al., Imaging the polar (0001) and non-polar (1010) surfaces of ZnO with STM, Surf. Sci. 415 (3) (1998) L1046–L1050.
[57] P. Mondal, Effect of Oxygen vacancy induced defect on the optical emission and excitonic lifetime of intrinsic ZnO, Opt. Mater. 98 (2019) 109476.